Wavefront control in space with MEMS deformable mirrors

Citation: Cahoy, Kerri L., Anne D. Marinan, Benjamin Novak, Caitlin Kerr, and Matthew Webber. “Wavefront control in space with MEMS deformable mirrors.” In MEMS Adaptive Optics VII, edited by Scot S. Olivier, Thomas G. Bifano, and Joel Kubby, 861708-861708-16. SPIE - International Society for Optical Engineering, 2013. © (2013) COPYRIGHT Society of Photo-Optical Instrumentation Engineers (SPIE)

Published Version: http://dx.doi.org/10.1117/12.2005685

Publisher: SPIE

Permanent Link: http://hdl.handle.net/1721.1/81180

Version: Final published version: final published article, as it appeared in a journal, conference proceedings, or other formally published context

Wavefront control in space with MEMS deformable mirrors

Kerri L. Cahoy*[a,b], Anne D. Marinan[a], Benjamin Novak[a], Caitlin Kerr[a], Matthew Webber[b]
[a]Dept. of Aeronautics and Astronautics, MIT, 77 Mass. Ave., Cambridge, MA, USA 02139; [b]Dept. of Earth and Planetary Science, MIT, 77 Mass. Ave., Cambridge, MA, USA 02139

ABSTRACT

To meet the high contrast requirement of 1×10^{-10} to image an Earth-like planet around a Sun-like star, space telescopes equipped with coronagraphs require wavefront control systems. Deformable mirrors (DMs) are a key element of a wavefront control system, as they correct for imperfections, thermal distortions, and diffraction that would otherwise corrupt the wavefront and ruin the contrast. The goal of the CubeSat Deformable Mirror technology demonstration mission is to test the ability of a microelectromechanical system (MEMS) deformable mirror to perform wavefront control on-orbit on a nanosatellite platform. In this paper, we consider two approaches for a MEMS deformable mirror technology demonstration payload that will fit within the mass, power, and volume constraints of a CubeSat: 1) a Michelson interferometer and 2) a Shack-Hartmann wavefront sensor. We clarify the constraints on the payload based on the resources required for supporting CubeSat subsystems drawn from subsystems that we have developed for a different CubeSat flight project. We discuss results from payload lab prototypes and their utility in defining mission requirements.

Keywords: adaptive optics, wavefront control, deformable mirror, high contrast, high dynamic range, CubeSat

1. INTRODUCTION

Scientists anticipated the existence of other Earth-like planets in the Universe well before the first discoveries of exoplanets by astronomers: pulsar planet PSR1257 + 12 [1] and 51 Pegasi b [2]. An Earth-like planet is normally thought of as a rocky planet with radius of 1-2 R_E (Earth radii), enough gravity to retain a substantial atmosphere, and located close enough to its parent star that liquid water could exist in a stable form on its surface. Implied in this definition is the ability of an Earth-like planet to support life.

This paper addresses the technology needed in order to directly image an Earth-like planet. Direct imaging of exoplanets is an example of a challenging new high contrast (~10^{10}), high dynamic range observation that seeks to identify an Earth-like planet around another star in the local solar neighborhood by measuring atmospheric absorption features in its reflected-light spectrum [3]. An Earth-like planet may be detected (as opposed to *characterized*) using methods other than direct imaging. Indeed, radial velocity and transit photometry observations have already delivered several promising candidates (e.g., the planets around Gliese 581 [4]; Kepler 22b, [5]; Tau Ceti e and f [6]). However, we address the challenge of *characterizing* an Earth-like planet, that is, observing how light from the parent star is reflected off of the Earth-like planet over a range of wavelengths [7]. These reflected light spectra contain continuum trends and absorption features that will not only tell us about the scattering properties, temperature, and pressure of the planet's atmosphere but also identify which gases are present and in what abundances (e.g., [8], [9] [10], [11], [12], [13], [14], [15]). Reflected light spectral information is key to determining whether or not these Earth-like planets contain life.

1.1 Direct Imaging Approach

In order to observe the reflected light spectrum of an Earth-like exoplanet, the instrument used must first be able to resolve the planet from the star and, second, have some way of "blocking" the parent star's light such that it does not saturate the detector and the reflected light from the orbiting exoplanet can be detected. The Rayleigh criterion of $\theta = 1.22\,\lambda/D$ describes the minimum angular separation between two monochromatic point sources that can be unambiguously resolved by a telescope with primary circular aperture of diameter D at wavelength λ. This is the angular separation of the first null in each point source's Airy function. The Airy function, or point spread function, describes the diffraction that occurs when the light from the point source passes through the circular aperture. The Airy function is a first order Bessel function of the first kind, J_1, and the number 1.22 is the first zero of J_1 divided by π. Angular resolution can be improved by increasing D or decreasing λ.

MEMS Adaptive Optics VII, edited by Scot S. Olivier, Thomas G. Bifano, Joel Kubby, Proc. of SPIE
Vol. 8617, 861708 · © 2013 SPIE · CCC code: 0277-786X/13/$18 · doi: 10.1117/12.2005685

An instrument called a coronagraph, originally developed to study the solar corona, uses an optical element to achieve the "blocking" of the parent star's light well enough that reflected light from an orbiting exoplanet can be detected. The coronagraph optical element can be as simple as an amplitude mask (e.g. [16], [3]), or it can be more complex and use both amplitude and phase to remove or relocate parent star's light ([17], [18], [19]). The coronagraph design must also consider the effect of the point spread function of each point source and the way that diffraction redistributes the light from the parent star across the image. High-performance coronagraphs are needed to achieve contrast ratios on the order of 1×10^{-10} in order to detect an Earth-like planet around a Sun-like star.

There are other proposed methods for obtaining spectra of Earth-like exoplanets. Some examples include "combined-light" spectra obtained from transit photometry observations (e.g., [20]) using an "external occulter" instead of an internal coronagraph (e.g., [21]), or using interferometry (e.g., [22] [23]). The transit photometry method takes advantage of the fact that at some point during a transit observation, the exoplanet travels behind its parent star. This is called a "secondary eclipse." When the planet is in secondary eclipse, the observation is only of the spectrum of the parent star. This can be compared with "combined-light" spectra that are obtained when both the planet and the parent star are in view. Challenges with this approach involve being able to discern the contribution of the reflected light from the planet from the much larger signal of the parent star, as well as understanding the variability of the parent star. The "external occulter" approach takes the occulting element from an "internal" coronagraph and places it at a large distance from the telescope. This approach requires precise manufacturing of the "starshade" used as the external occulting element as well as precise control of the starshade position. Interferometers can also be used as a type of single internal coronagraph or employed across multiple spacecraft in a distributed approach. In this paper, we focus on technologies that apply to the "internal coronagraph" direct imaging method.

The stated 1×10^{-10} contrast ratio can be straightforwardly calculated. The contrast ratio between an exoplanet and its star depends on many factors, including the physical properties of the planet and star, the system geometry, background sources, and the instrumentation used. A simple way of estimating the required contrast is to assume that the planet reflects its incident starlight isotropically. Thus its apparent brightness is constant over its illuminated surface, like a Lambertian surface. Then, the contrast can be expressed as [24]:

$$C(\alpha) = \frac{2}{3} A_g(\lambda) \left(\frac{R_p}{d}\right)^2 \left[\frac{sin(\alpha) + (\pi - \alpha)cos(\alpha)}{\pi}\right],$$

where α is the planet phase angle, R_p is the planet radius in km, d is the planet–star separation in km, and A_g is the geometric albedo. The geometric albedo generally takes values between 0 and 1 for the fraction of monochromatic light the planet reflects toward the observer at full phase at wavelength λ, although it can be larger than 1 for anisotropic scattering atmospheres or surfaces. If one assumes that the planet is at quadrature, $\alpha = \pi/2$, and that the geometric albedo at the wavelength of interest is 0.5, then for a Jupiter analog (1 R_J), the contrast at 0.8 AU is $\sim 3.8 \times 10^{-8}$ and at 10 AU is $\sim 2.4 \times 10^{-10}$. For a Neptune analog (1 R_N), the contrast at 0.8 AU is $\sim 4.5 \times 10^{-9}$ and at 10 AU is $\sim 3 \times 10^{-11}$. For an Earth analog (1 R_E) at 1 AU with $A_g = 0.3$, the contrast is $\sim 1.2 \times 10^{-10}$ [12]. High contrast is more difficult to achieve closer to the star than further away, but the d^{-2} dependence also means that planets further from the star will be fainter in reflected light.

1.2 Role of Deformable Mirrors in Exoplanet Direct Imaging Systems

Thus, in order to image an Earth-like planet, an exoplanet direct imaging system needs to achieve a contrast ratio of 1×10^{-10}. A high-performance coronagraph is designed to meet this requirement. However, in addition to the challenge of atmospheric turbulence for a ground-based telescope, even the performance of a space telescope will still suffer from optical imperfections, thermal distortions, and diffraction that will corrupt the wavefront, create speckles, and ruin the contrast.

Adaptive optics systems that compensate for atmospheric turbulence (typically characterized by Fried parameter r_0 and Greenwood frequency τ_0) are designed to perform at higher speeds and with larger strokes than that needed by wavefront control systems on space telescopes used for astronomical observations that do not need to compensate for atmospheric turbulence. On the ground, a two-mirror woofer-tweeter (coarse-fine) wavefront control approach is frequently used [25] where the woofer corrects slower, larger amplitude, lower-frequency components and the tweeter corrects faster, smaller-amplitude, higher-frequency components. In this paper, our proposed deformable mirror demonstration mission

focuses on developing a low-cost, easy-access-to-space platform for validating technologies used for the tweeters: more complex, higher actuator count deformable mirrors.

The need for high actuator count deformable mirrors for an exoplanet direct imaging mission is to extend the angular separation from an on-axis star where we can look for an exoplanet and extend the region over which the deformable mirror has the authority to compensate for speckles and aberrations. If a deformable mirror only has a few actuators, it can only correct for low spatial frequencies that are close to on-axis in the image plane, corresponding to larger-scale distortions in the pupil plane. To be able to correct for speckles and aberrations "further out" around a star so that we can look for exoplanets in the region known as the habitable zone, it is necessary to have mirrors with more actuators and the corresponding control over higher spatial frequencies (further off-axis in the image plane).

1.3 Space Telescopes for Direct Imaging

It is desirable to use a space telescope for Earth-like exoplanet observations (as opposed to observations of larger and brighter gas or ice giant exoplanets) because even for ground-based telescopes with high performance adaptive optics systems [26] and an ideal coronagraph, the speed of atmospheric turbulence and the limited number of photons from the exoplanet target, in addition to constraints on viewing geometry and integration time, limit the achievable contrast. Observations that can capture features in the atmospheric spectra of an Earth-like exoplanet require wavefront control because even a well-engineered space telescope with a sophisticated high performance coronagraph [16] [27] will have mid and high spatial frequency wavefront aberrations that will degrade the achievable image contrast [28] [29] [17]. Drifts in the optics shapes over the long integration times necessary for such a scientific observation should be comparatively small and slow, thus wavefront control techniques can be used to reduce the phase errors to an acceptable level (for example, less than 1 nm). Wavefront control systems are also needed to manage speckles that result from diffraction, phase errors, and noise. In cooperation with the spacecraft attitude determination and control system (ADCS), wavefront control systems can also be used to address sub-milliarcsecond pointing errors [30]. The spacecraft ADCS system is designed to provide "coarse pointing" which is on the order of the angular resolution of the system over periods of time that are shorter than twice the desired integration time. Structural vibrations from reaction wheel imbalances during momentum management may introduce angular motions that exceed the angular resolution over twice the desired integration time. The imaging detector may also be actively cooled to help reduce thermal noise (dark current), and the cyclic cryo-coolers used may also induce angular disturbances. In order to achieve the fine pointing requirements, the optical system design is as structurally isolated as possible, and fast steering mirrors are typically used to reduce the impact of vibrations.

1.4 Goals of the CubeSat Deformable Mirror demonstration

The development of a space telescope equipped with a high performance coronagraph and deformable-mirror wavefront control system that is capable of the 1×10^{-10} contrast needed to directly image Earth-like exoplanets is expected to be on the order of several hundreds of millions of dollars to over a billion dollars. The goal of the CubeSat Deformable Mirror Demonstration is to provide a low-cost way to quickly test small, low-power, higher actuator-count deformable mirror technologies on-orbit and raise their technology readiness level (TRL) for use on larger, more capable space telescopes. While several important environmental tests can be performed using these mirrors on the ground (thermal vacuum, vibration, life cycle testing, and to a limited extent, radiation), it is important to demonstrate that simple wavefront control systems utilizing new deformable mirror technologies have stable, well-calibrated, and predictable performance on orbit. This is particularly important to emphasize, as there is no opportunity to "tweak" or "adjust" a wavefront control system on orbit after launch. It is of particular importance to fully develop robust flight software to control these mirrors and systems, to incorporate them as sensors with spacecraft ADCS, estimators, and fine pointing algorithms, and to determine how best to capture performance and calibration data along with science observations and transmit it to the ground.

1.5 Background on the CubeSat Platform

The CubeSat form factor was developed by California Polytechnic Institute (CalPoly) and Stanford University in 1999. It interfaces with a common secondary payload deployer, the Poly-picosatellite Orbital Deployer (P-POD), which significantly reduces the cost and time for obtaining launch opportunities for nanosatellites. The basic nanosatellite unit is a 10 x 10 x 10 cm cube (called 1U). The P-POD unit will support a 3U volume in a variety of combinations [31]. For example, it can accommodate three 1U CubeSats. Or, it can accommodate a single triple-long 3U CubeSat (which can be about 34.05 cm long instead of 30 cm, since space allocated for "feet" separating individual 1U CubeSats can be allocated to the volume of the single 3U). CubeSats are usually launched as secondary payloads on government or

commercial primary missions, with their launch accommodation often sponsored by government agencies, such as the NASA Educational Launch of Nanosatellites (ELaNa) program. A 3U CubeSat is an appropriate platform for the Deformable Mirror Demonstration mission because it enables a comparatively quick, simple, low-cost approach for a technology demonstration whose results would have significant impacts on the design, scale, and capabilities of future space-based optical systems.

2. PAYLOAD FOR THE CUBESAT DEFORMABLE MIRROR DEMONSTRATION MISSION

The purpose of this section is to describe two concepts for a 3U CubeSat platform that demonstrate MEMS deformable mirror technology and increase the TRL of a miniaturized, low-power, standalone wavefront control system for a space telescope:

- Payload concept 1: Miniature Michelson interferometer
- Payload concept 2: Shack-Hartmann wavefront sensor

Both of these concepts are in preliminary stages of development and will benefit from community input and lab demonstrations. The initial demonstration mission design is kept as simple as possible; in the future additional CubeSats can be flown to perform demonstrations with increased complexity and functionality. The supporting spacecraft subsystems for the 3U CubeSat are described in greater detail in Section 3. For the purpose of evaluating payloads, we assume the following constraints on the payload mass, volume, power, and data rate:

- Mass < 1.5 kg
- Volume < 1.5U (15 × 10 × 10 cm)
- Average Power < 5 W
- Data rate < 120 Mbits/day

The remaining resources of the 3U CubeSat are required for communications, attitude determination and control, power, command and data handling, and thermal subsystems.

2.1 Payload Requirements

While much work remains to be done to better define payload performance requirements, for the purpose of this feasibility evaluation, the payload shall be able to:

1. Demonstrate that high actuator count MEMS deformable mirrors can be commanded and controlled on-orbit for one month (minimum), 12 months (goal).
2. Use a simple static wavefront sensing system (such as interferometric, shear, or mask [32], [33]) to characterize the performance of the MEMS mirror. This includes evaluation of:
    a. Individual actuators
    b. Multiple actuators contributing to mirror shapes such as tilt, Fourier, and Zernike modes (zonal and modal sensing [32])
3. Demonstrate closed-loop control of mirror shape over integration times from 100 seconds to 1,000 seconds in the presence of:
    a. Thermal gradients
    b. Attitude control jitter

It is important to keep in mind that this mission is to demonstrate functionality of a MEMS deformable mirror in a simple wavefront control system on orbit. It would add complexity and cost to levy exacting phase correction requirements on the system, although such an approach would be an appropriate advance in a follow-on mission.

2.2 Payload design trades

To meet the mission goals and keep costs low, the approach is to use as much existing commercial off the shelf (COTS) hardware as possible, making modifications as needed for operation in space, and to keep the design as simple as possible. We avoid mechanisms other than the deformable mirror itself to eliminate additional complexity and risk.

2.2.1 Internal or external light source

One major design trade is whether to use an internal (diode laser), an external (bright star) light source, or both. The current mission objectives and payload requirements can be met using an internal laser as the light source. This would

reduce cost and complexity since the attitude determination and control (ADCS) system would not need to maintain pointing at a star for long periods of time, which would require the use of a miniature CubeSat-sized reaction wheel assembly. The power requirement needed by a reaction wheel assembly is about 4 W. With an internal source, the ADCS system could meet pointing requirements to Earth ground stations for communication downlink using only magnetic torque coils or rods. Use of a laser would also be beneficial for routine calibration of the system. The power requirement of the laser is < 0.5 W for a ~5 mW laser. A neutral density filter would be also needed to attenuate the laser signal so that it does not saturate the detector.

Having considered the benefits of using a diode laser as an internal light source, there is still the ultimate goal of using this technology on space telescopes that motivates the use of an external light source, namely, a bright star. There are two approaches to imaging a star. One is to know what star we want to point at and navigating there, and this would require a CubeSat-sized star tracker along with coarse (reaction wheels) and fine (steering mirror or device) attitude control actuators. Another approach is to image stars but not be particular about what is being imaged. Either way, imaging a star would drive the CubeSat system design in a way that would bring value to future wavefront sensing space telescope missions, such as developing the ADCS algorithms that include both pointing and closed-loop wavefront control. The question for a simple CubeSat demonstration mission is whether coarse actuators such as the reaction wheel assembly and magnetorquers is sufficient to keep a bright star within the field of view (FOV) of the detector for over a minute, since having additional actuated elements are outside of the mission scope. If it is not necessary to steer the spacecraft to a specific star or to identify the star - not required to achieve the objectives of this technology demonstration - then simple algorithms that identify the presence of a bright object on the detector and center it would be sufficient. One goal of this feasibility study is to establish whether or not a fast steering (tip-tilt) mirror will be needed on a CubeSat technology demonstration platform that images specific stars. It is generally accepted that a fast steering mirror will be needed on a larger space telescope. The fast steering mirror would allow for much more accurate pointing than a reaction wheel assembly can provide, and would also correct for tip and tilt errors in the wavefront that may be larger than the stroke of the deformable mirrors can correct for. Estimates of pointing control for a CubeSat sized reaction wheel assembly alone are ~60 arcseconds (3σ) [34] [35]. Additional work to evaluate the combined pointing accuracy needs of the optical system and capabilities of the CubeSat is needed for the proposed payload designs.

If an external light source is used, the aperture would necessarily be small given the CubeSat size constraints. As discussed in Section 3, not much space remains after accommodating the key elements of the system (deformable mirror, mirror drive electronics, imaging optics, and detector). Due to the need to accommodate a deformable mirror and reduce complexity, it is not practical to try to design the CubeSat as a reflecting telescope using mirrors. While it may be possible to integrate a larger standard lens in the aperture (up to 75 mm diameter may be feasible in a 3U CubeSat), the corresponding longer focal length (> 75.0 mm) is not an option due to the limited space available for all components, and resizing the beam would be difficult. A smaller aperture and lens will limit the angular resolution (~1.22 λ/D) and sensitivity as well as increase the size of the PSF (which must also be Nyquist sampled by the pixels on the detector), but tight angular resolution is not a requirement for this technology demonstration. For a 1-inch (25.4 mm) or ½-inch lens (12.7 mm) diameter lens, which have a minimum focal length on the order of their diameter, the angular resolution (width of the center of the point spread function) at 500 nm would be 1.2 arcseconds (1-inch) and 2.4 arcseconds (½-inch).

2.2.2 MEMS Deformable Mirrors

Even though MEMS deformable mirrors themselves are quite small, a widely acknowledged challenge to incorporating high actuator count deformable mirror systems on a spacecraft is the substantial size, mass, volume, power, and complexity of the mirror driver boards and wire harnesses [36] [28]. While development of application-specific integrated circuit (ASIC) drivers is a current focus of several deformable mirror manufacturers [37] [38], it is uncertain when ASIC drivers will become generally available and whether they will be appropriate for space applications. For the purpose of this technology demonstration, both the mirror and driver need to fit within the payload constraints as well as leave space for supporting optics and a detector. We are still investigating the ability of candidate mirror and driver systems from manufacturers such as Boston Micromachines Corporation (BMC), Iris AO and Xinetics. We have currently identified and started laboratory experiments with a candidate DM, the 32-actuator "Mini" from Boston Micromachines, where both the DM and existing drive electronics board fit in the 1.5U payload volume of a 3U CubeSat without significant modification. We have also confirmed that with some minor modification to the drive electronics board, the Iris AO PTT111 (37 segment mirror) would fit as well. The baseline CubeSat deformable mirror payload design discussed here accommodates a BMC "Mini" deformable mirror from Boston Micromachines [39] with their new

mirror housing design (dimensions roughly 50 mm diameter × 22.1 mm tall, note that the earlier model was 114.17 mm × 74.93 mm × 70.99 mm and would not fit [40]). The BMC Mini is a 6 x 6 deformable mirror (32-actuator, as the four corners are not active). There are three different stroke and aperture options with the Mini, as summarized in Table 1. There are trades to be further examined between stroke for non-atmospheric wavefront correction versus response time, pitch, and interactuator coupling. Having a larger stroke without increasing the number of possible voltage steps (bits in the digital to analog converter) also reduces the precision to which the actuators can be controlled.

Table 1: Boston Micromachines Mini MEMS deformable mirror options [39]

Stroke	1.5 μm	3.5 μm	5.5 μm
Aperture	1.5 mm	2.0 mm	2.25 mm
Pitch	300 μm	400 μm	450 μm
Approx. Mechanical Response Time (10%—90%)	20 μs	100 μs	500 μs
Approx. Interactuator Coupling (+/-5%)	15%	13%	22%

The Mini DM has 14 bit step resolution and a sub-nm average step size. The fill factor is >99%, the surface finish is < 20 nm RMS, and the driver is completely powered and controlled by a USB 2.0 interface. The frame rate is 8 kHz, with a 34 kHz burst mode. As noted, the most recently available BMC Mini packaging format is selected (5 cm diameter and 2.21 cm tall, 75 g without cables). The existing Mini driver board has dimensions of 13 × 10 × 1.8 cm, and there is bare, unused printed circuit board for ~2.75 mm on each side of the width dimension, such that the board could have dimensions 13 × 9.5 × 1.8 cm. The initial plan is to use this board and make as few modifications as possible to the board and device (e.g. remove windows on the mirror before flight, replace electrolytic capacitors on the boards, etc.), apply conformal coating, and secure connectors.

Figure 1: Boston Micromachines Mini 6 × 6 (32 actuator) deformable mirror and drive electronics [39]. The drive electronics board would be used without the packaging and with some minor modifications to the board.

2.2.3 Wavefront sensors

There are many different approaches to wavefront sensing and reconstruction. To start with, there are both sensored and sensorless approaches, the former having the challenge of a non-common optical path with the detector, and the latter requiring additional computational resources, time, and sometimes additional detectors or detector translation (such as Gerchberg-Saxton, phase diversity, or "lucky" imaging). For the exoplanet direct imaging application on a large space telescope mission, it is likely that a sensorless approach will be used to eliminate non-common path optical errors. However, since the first goal in this work is mirror characterization and we do not expect to have a platform with the same stability and processing capability as a dedicated exoplanet direct imaging mission, in this work we focus on two approaches to wavefront sensing selected from among several established methods [32] because they can be simply implemented in a compact form factor without additional mechanisms such as rotating or translating components. Another important aspect to consider is the robustness of the sensor given the need to survive launch and function without intervention from on-orbit. The two approaches discussed in detail here are versions of: (1) a Michelson interferometer and (2) a Shack-Hartmann wavefront sensor. There are additional wavefront sensing approaches that could be implemented, such as using an aperture mask to augment sensorless approaches, as well as improved or modified versions of the lenslet and shear sensing approaches that we investigate here, that we will consider in future work. One example of this is a point diffraction interferometer [41], which could be used in place of a Michelson interferometer if the low light efficiency and decreased performance in conditions of high aberration are acceptable.

2.3 Concept 1: Michelson Interferometer

The Michelson interferometer concept is well known and has a variety of applications including wavefront sensing [32], [42]. While interferometry can be used for precise characterization of optical surfaces, the purpose of this experiment is to evaluate to what extent a simpler, smaller CubeSat-sized system would work, first for evaluating basic mirror functionality and next, how well it would work for characterization of mirror performance. Figure 2 shows a Michelson interferometer setup that incorporates a MEMS DM. The laser light encounters a beam splitter (BS). The transmitted beam travels to the MEMS deformable mirror where it is reflected back to the beam splitter. Half of this beam is deflected by 90 degrees at the BS and strikes the detector. The other part of the beam travels to a flat mirror, where it is reflected back to the beam splitter. Half of this light then passes straight through the BS and reaches the detector. The two beams that are directed towards the detector interfere to produce fringes that are analytically well understood as a function of beam coherence, divergence and mirror angle (tip/tilt) [43] [32] [42]. Fringe patterns can be simulated and demonstrated for a variety of other different mirror shapes and positions. Additional elements such as a pinhole filter, neutral density filter, and imaging lens are not shown in Figure 2. Optical elements used in the payload would be selected and designed to survive the radiation environment, thermal environment, and launch and deployment shock and vibration, such as using UV-grade fused silica lenses with stress-free mounts in multi-point supported lens tubes. Several of these mounts would need to be custom made. The components will be housed within a black enclosure to eliminate stray light from the spacecraft bus.

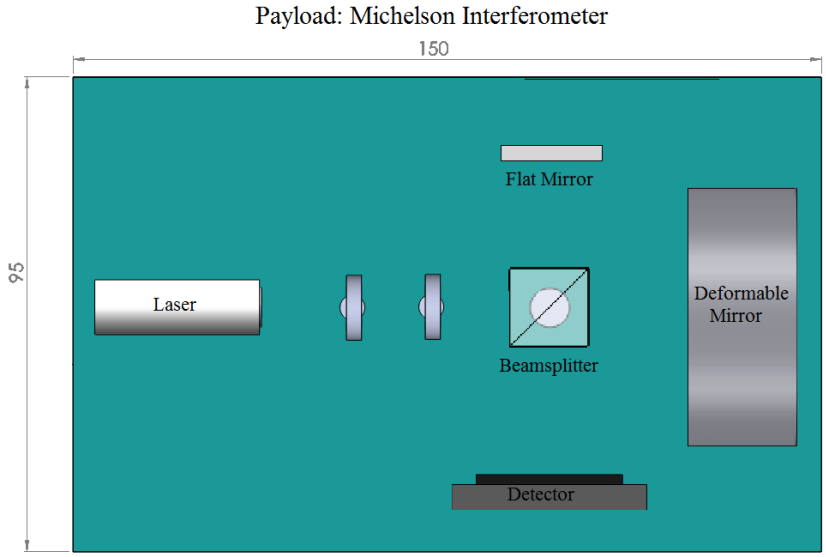

Figure 2: Rendering of a CubeSat-sized Michelson interferometer with a MEMS deformable mirror and internal light source (diode laser). Dimensions are in millimeters. The beam splitter (BS) divides the laser beam. The transmitted beam is collimated and travels to the MEMS deformable mirror where it is reflected back to the beam splitter. Half of the beam is deflected by 90 degrees at the BS and strikes the detector. The reflected beam travels to the flat mirror where it is reflected, and half passes straight through the BS to the detector where it interferes with the light going directly from the DM to the detector, producing fringes that are analytically well understood as a function of beam coherence, divergence and mirror angle (tip/tilt) [43] [32]. Interference fringes can be simulated and demonstrated for a variety of other different deformable mirror shapes. Additional elements, such as a pinhole for spatial filtering of the wavefront, a neutral density filter, and imaging lens were used in the laboratory demonstration. The distance between the flat mirror, DM, and detector can vary.

Fringes from the interferometer can be generated both from a collimated source (straight fringes) or from a spherical point source that is diverging (radial fringes) [42]. When the flatness or shape of a mirror changes, the resulting

interference pattern is affected by changes as small as fractions of a wavelength. For basic piston and tip/tilt modes, it is straightforward to determine how well the deformable mirror is performing by studying the fringes in the images captured by the detector. For example, for a collimated beam, if the entire deformable mirror surface tilts by an angle θ from its original normal, the observed fringes occur at intervals of $\Delta x' = 2\lambda/\sin(\theta)$. If the deformable mirror surface moves forward (piston) by distance Δd, the observed fringe pattern moves as Δd changes, and the number of fringes that cross the center of the screen is $n = 2\Delta d/\lambda$.

(a) CubeSat-scale MEMS DM Michelson interferometer *(b) "Flat" deformable mirror fringes.*

Figure 3: CubeSat-sized MEMS DM Michelson interferometer experiment, initial tip-tilt results. (a) The setup includes a 1.5 micron stroke Boston Micromachines Mini deformable mirror, a Thorlabs CPS180 635 nm 1 mW round beam collimated laser diode module, a cube beam splitter, a pinhole spatial filter, a neutral density filter, a flat mirror, and a Thorlabs DCC1545M ½" monochrome CMOS camera. A Matlab interface to the mirror driver is commanding the 32 actuators into a "tilt" or "tip". (b) The interference pattern when the MEMS deformable mirror is set to "flat". The radial fringes indicate that the beam is not quite perfectly collimated.

Figure 3 shows the laboratory setup and initial tip-tilt results from a CubeSat-sized MEMS DM Michelson interferometer. The setup includes a 1.5 micron stroke Boston Micromachines Mini deformable mirror, a Thorlabs CPS180 635 nm 1 mW collimated laser diode module, a cube beam splitter (which will distort less than thinner beam splitters and has the added benefit of the coating being sealed inside the cube), a pinhole spatial filter, a neutral density filter, a flat mirror, and a Thorlabs DCC1545M ½" monochrome CMOS camera. A Matlab interface to the mirror driver commands the 32 actuators into a "tilt" or "tip". Algorithms to analyze the images and fringe patterns compared with the DM commands are currently being tested.

2.4 Concept 2: Shack-Hartmann Wavefront Sensor

The Shack-Hartmann wavefront sensor is also well known in the field of adaptive optics and its basic concept appears to have predated even the Michelson interferometer [44]. The Shack-Hartmann sensor uses an array of lenslets across the pupil which all have the same focal length that are projected onto a detector. Each lenslet samples the local tilt of the wavefront, and this is evident in the position of that lenslet's focal spot on the detector. Any shape phase aberration of the whole wavefront is measured as a set of discrete tilts as measured by the lenslet array. Since only slopes are measured, the Shack-Hartmann cannot detect discontinuous steps in the wavefront.

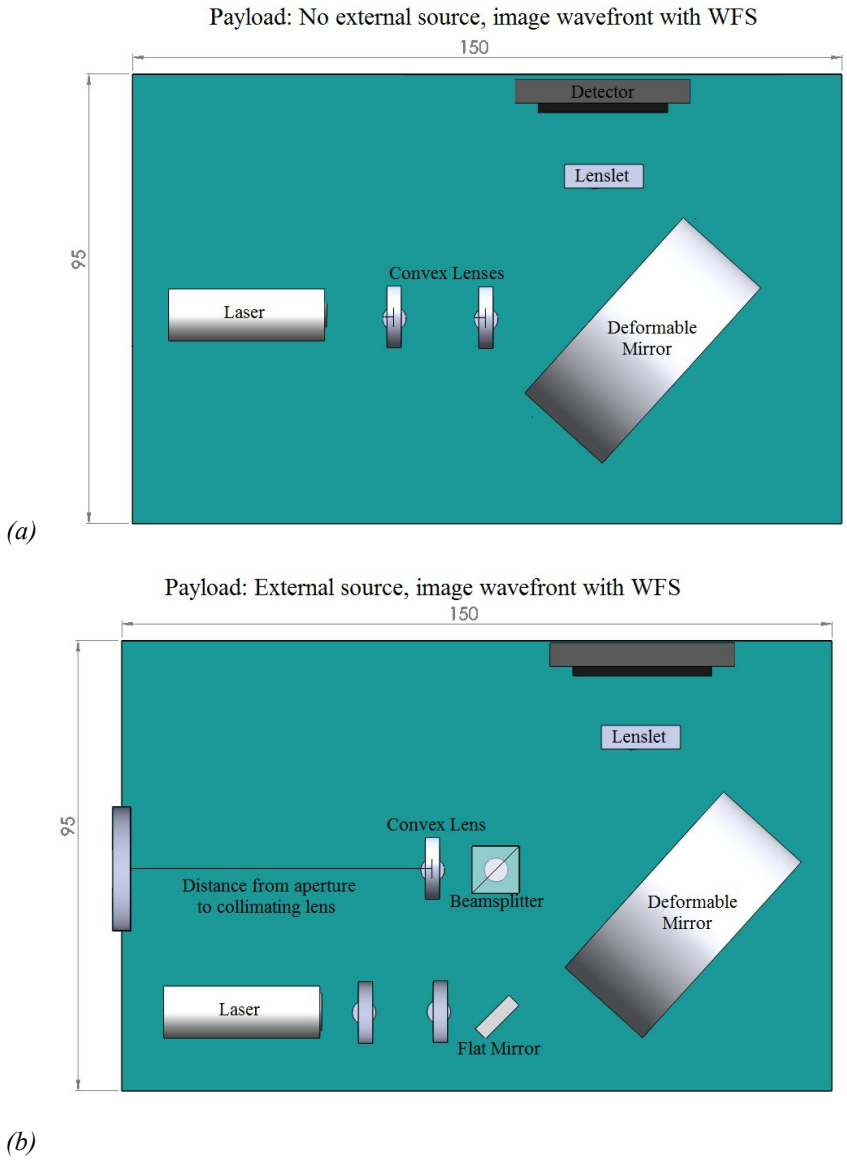

Figure 4: Rendering of a CubeSat-sized Shack-Hartmann wavefront sensor with a MEMS deformable mirror and (a) internal light source and (b) with both an internal light source (diode laser) and external source ½-inch f=50 mm lens. Dimensions are in millimeters. The ½-inch f=50 mm lens is paired with a 6 mm diameter f=10 mm lens to resize the beam to approach the ~2 mm deformable mirror aperture. A lenslet array is used to image the pupil plane onto the detector. The diode laser can be turned on to dominate the system at any time, using resizing optics to fill the same aperture going from the DM to the Shack-Hartmann (SH) wavefront sensor.

Figure 4 shows renderings of a CubeSat MEMS DM payload using a Shack-Hartman wavefront sensor for an internal light source (a) as well as both an internal light source and aperture (b). In configuration (b), the characterization of the mirror using the internal light source could be done first, and then once the primary mission goals are satisfied, the laser could be turned off and objects from the aperture could be observed. The laser would be coherent and orders of magnitude brighter than any star in the aperture.

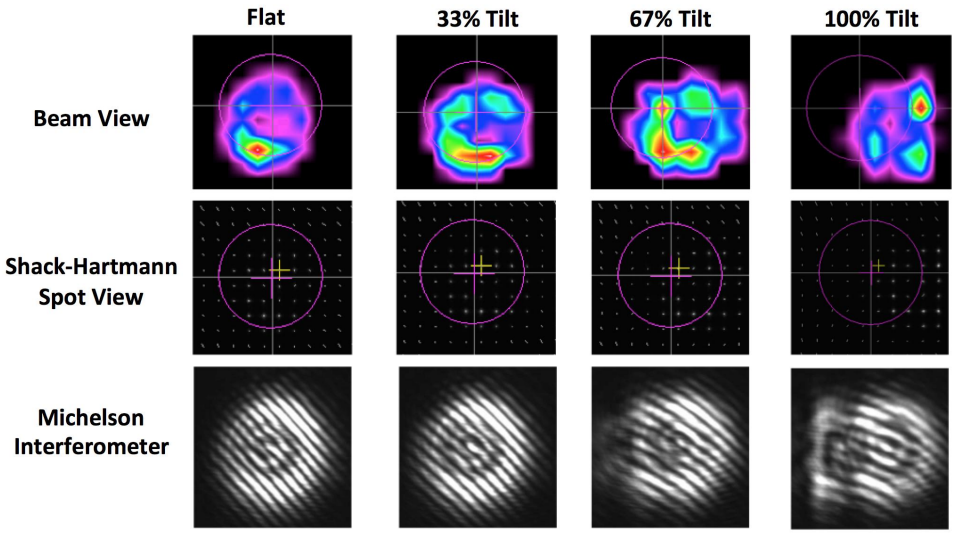

Figure 5: Example results looking at different steepness tilts on the MEMS DM. The "beam view" is the laser intensity as reflected off of the MEMS deformable mirror, the "Shack-Hartmann spot view" shows the lenslet focal spot locations and intensities, and the Michelson interferometer shows fringes (note that if the beam is perfectly collimated, there should not be any radial fringes).

Figure 5 shows the intensity measurement, Shack-Hartmann spots, and Michelson interferometer fringes observed when the MEMS DM is commanded to perform an effective tilt. The percent tilt is in terms of the maximum displacement of the actuator. A tilt of 33% means that the actuators on the furthest side of the tilt are at 33% of their maximum allowed displacement. Software to analyze the fringe patterns and infer mirror commands is currently under development.

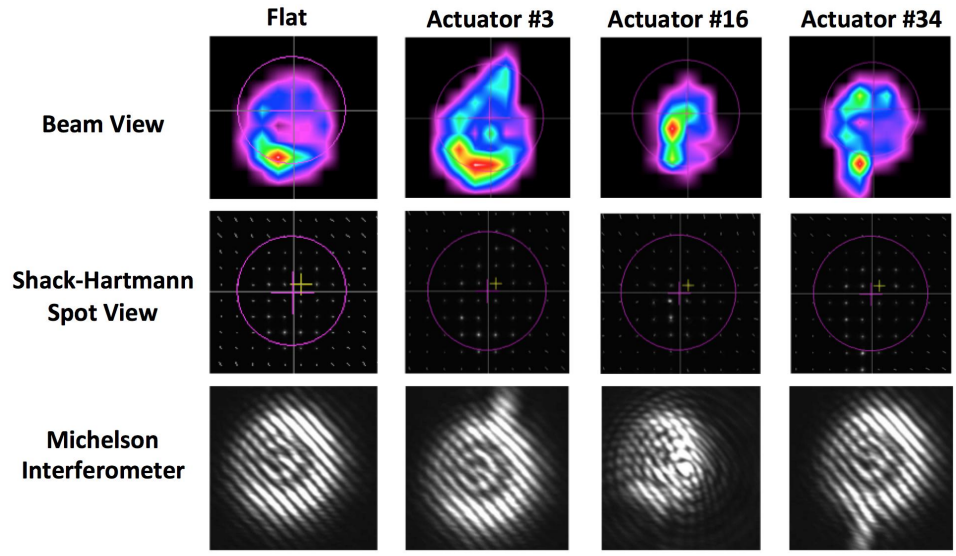

Figure 6: Example results looking at different actuator "pokes" on the MEMS DM. The "beam view" is the laser intensity as reflected off of the MEMS deformable mirror, the "Shack-Hartmann spot view" shows the lenslet focal spot locations and intensities, and the Michelson interferometer shows fringes (note that if the beam is perfectly collimated, there should not be any radial fringes).

In Figure 6, individual actuators were commanded to their maximum allowed displacement level. Different shapes were commanded to the mirror in Figure 7, namely three different Zernike polynomials. Given the square aperture and organization of the actuators for the BMC Mini DM, it would probably be best to use Fourier modes for characterization of the mirror in future work.

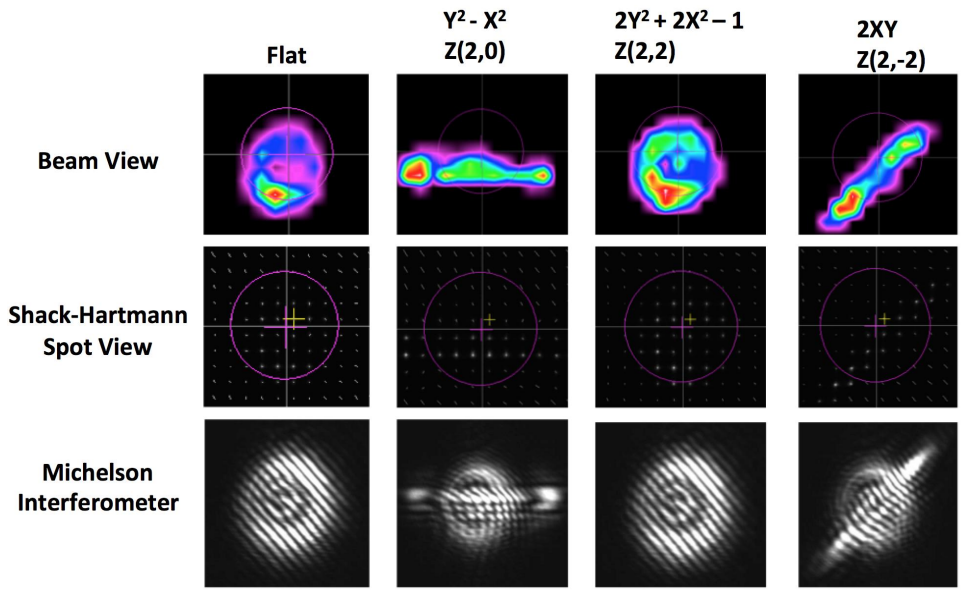

Figure 7: Example results looking at different Zernike polynomials on the MEMS DM. The "beam view" is the laser intensity as reflected off of the MEMS deformable mirror, the "Shack-Hartmann spot view" shows the lenslet focal spot locations and intensities, and the Michelson interferometer shows fringes (note that if the beam is perfectly collimated, there should not be any radial fringes).

The initial results shown in Figure 5 through Figure 7 show that different types of commands to the MEMS DM can be captured and are fairly easily distinguishable from each other by either a Shack-Hartmann wavefront sensor or Michelson interferometer, although much work remains in order to quantify the response of the mirror to commands as detected by the sensing system.

2.4.1 Concept of Operations

The use of an internal light source for the initial demonstration of DM functionality on-orbit eliminates any payload-specific requirements on the CubeSat's altitude and inclination. The orbit altitude range of 400 to 600 km is limited on the upper constraint by the CubeSat maximum de-orbit time requirement and on the lower constraint by drag and the desired mission lifetime of one year. A high-level overview of the concept of operations includes phases for launch, deployment, and detumbling, thirty days of commissioning, and a success threshold of one month of nominal operations and data downlink with a goal of twelve months of nominal operations and data downlink. The first phase of nominal operations involves open-loop wavefront sensing of a repeating sequence of mirror surface shapes during which characterization and calibration is performed. This is followed by the second phase of the mission, closed-loop wavefront sensing, where the CubeSat microcontroller is used to achieve and maintain a desired surface shape on the DM. This is followed by a third phase whose purpose is to simulate the effects of bad actuators and increasingly noisy signals before deorbiting.

3. CUBESAT SUBSYSTEMS

3.1 Power

Two solar panel configurations were modeled in STK: (i) a set of four 3U body-mounted panels, shown in Figure 4, and (ii) a set of four two-sided 3U deployed solar panels and no body-mounted panels. Each 3U surface holds 7 ultra-triple junction solar cells. In each case, the spacecraft is oriented with the long axis parallel to the zenith-nadir line. The results from power generation calculations for a series of orbital altitudes and inclinations for each configuration for one orbit are shown in Table 2, which compares the orbit-averaged power (averaged over daylight, non-zero power generation) for each case. Simulations show that the while peak power generation is generally higher with the deployed panels, the body-mounted panels provide more uniform power generation pattern across the orbit.

Table 2: Orbit average generated power

Orbital Inclination (degrees)	Orbital Altitude (km)	4 x 3U Body-Mounted Panels Orbit Avg. Generated Power (W)	4 x two-sided 3U Deployed Panels Orbit Avg. Generated Power (W)
0	300	12.3	12.0
0	400	12.4	11.9
0	500	12.2	11.8
45	300	11.9	12.1
45	400	12.2	12.1
45	500	12.2	12.1
90	300	14.8	6.2
90	400	15.0	6.4
90	500	15.0	6.4

While the peak power generation is higher with the deployed solar panel configuration, a calculation of the orbit-averaged power shows that the body-mounted panel generation is more favorable than that of the deployed panels for the a mission where the body-mounted solar panels will not be obstructed, for example, due to the presence of an antenna, sensor, or instrument field of view. Using only deployed panels does not provide a significant increase in power generation; it makes for a less consistent power profile, and deployed panels add unnecessary complexity and cost to the spacecraft. For these reasons, the current design utilizes four 3U body-mounted panels.

If further analysis shows that more power generation is required, additional options can be considered. One is to utilize deployed panels in conjunction with body-mounted panels. Another is to design the spacecraft to enable solar array sun-tracking, which would require a more robust ADCS design, articulated solar panels, or both.

3.2 Structure

The basic structure of the spacecraft is a 3U CubeSat with body-mounted solar panels. Figure 8 shows two views of the spacecraft: one showing the 3U skeleton with volume-representative parts, and one showing the outer solar panel structure.

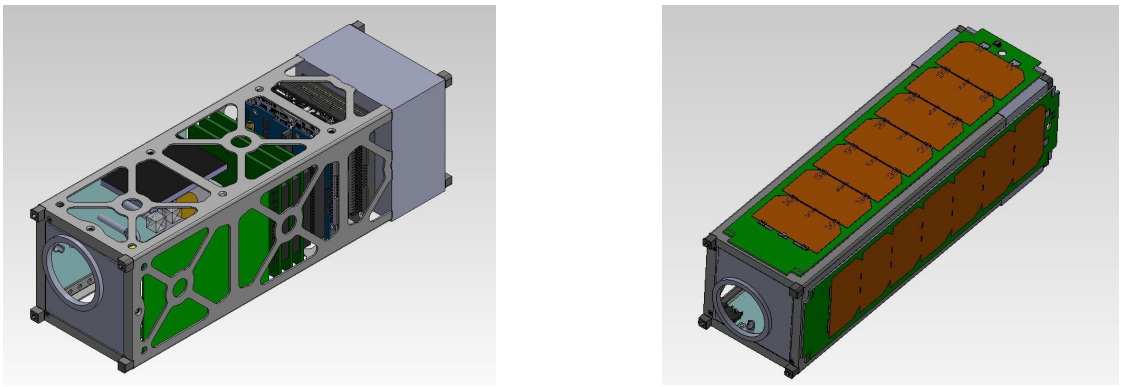

Figure 8: All components will be housed inside a 3U CubeSat (left) with body-mounted solar panels covering the outer walls (right). Antennas for communication would be mounted on the sides or nadir face of the structure, which would be maintained in a gravity gradient orientation (with the aperture zenith pointing).

A preliminary placement of the subsystem boards and payloads within the 3U CubeSat volume is shown in Figure 9. The microcontroller and motherboards are from Pumpkin Inc., the batteries and electrical power system (EPS) are from Clyde Space, and the structure is a Pumpkin 3U skeletonized chassis. The communications system is a UHF Cadet nanosatellite radio from L-3 Communication Systems West. The payload takes up a volume of approximately 1.5U.

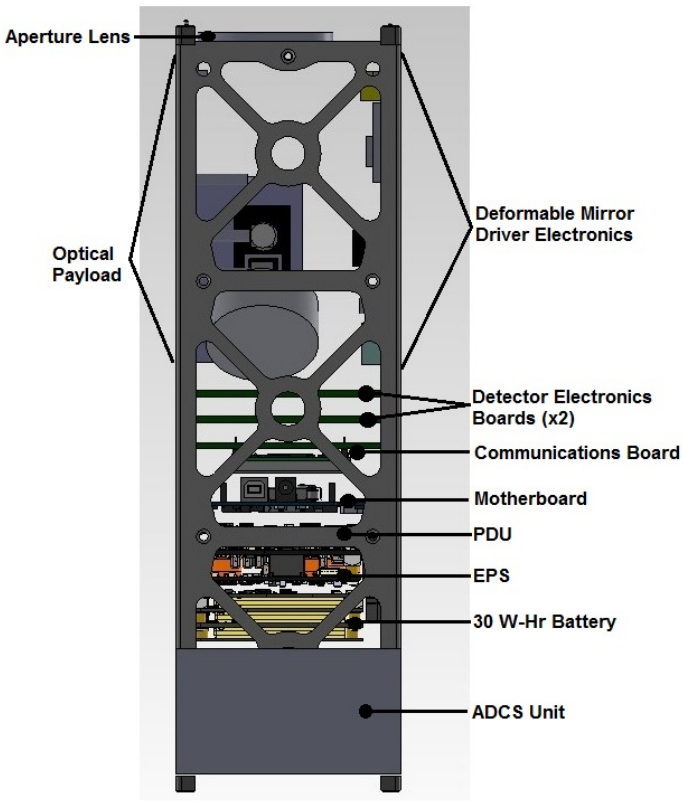

Figure 9: Subsystems stack and payload accommodation in the 3U CubeSat.

3.3 ADCS

The Attitude Determination and Control System (ADCS) for the internal light source design needs only to achieve pointing toward a ground station for communication. The payload is housed entirely within the bus structure and its operability is not affected by the attitude or orientation of the spacecraft (although sensitivity to disturbances is another area under study). Referencing an example flown on previous CubeSat missions [45], a simple approach for the ADCS system is passive magnetic control. A sensor package of a magnetometer, IMU, and coarse sun sensors would satisfy the relatively flexible pointing requirements of a mission that used an internal source (1 to 10 degrees, depending on the inclination and variability of the magnetic field).

Pointing the CubeSat at a particular star and maintaining lock on that star for an observation would require a substantial amount of additional cost and complexity to the mission. Currently available reaction wheel assemblies with CMOS or infrared (thermopile) Earth horizon sensors are not anticipated to achieve better than 0.5 degrees of pointing knowledge. A star tracker and multi-stage control system could improve this to possibly as good as 1 arcminute, however, COTS CubeSat reaction wheel assemblies with star trackers are not yet available (and are anticipated to be at a higher price point than existing reaction wheel assemblies).

3.4 Thermal

The baseline thermal design is a passive system with the exception of the Clyde Space battery, which includes internal heaters. A comprehensive thermal model of the satellite and a more in-depth analysis of the payload components will determine the need for active thermal management. Small flexible heater circuits, such as those from Minco, may be required for spot thermal management, such as near the Thorlabs CPS405 laser diode (however, the CPS405 is engineered to survive -40 to 80° C and operate in -10 to 40° C).

3.5 Communications

The communications system will consist of Cadet nanosatellite UHF radio from Level 3 Communications West. The UHF radio board is half-duplex and will use amateur radio frequencies in the 445 to 455 MHz (uplink) and 460 to 470 MHz downlink. Ground stations such as the 18 meter dish at NASA Wallops would enable a robust communications link and a sufficient rate of data downlink.

3.6 Payload components

Examples of some COTS payload components includes a collimated laser diode such as the CPS405 from Thorlabs, a 4.5 mW, 405 nm laser which takes 5 VDC regulated power and has a -10° to 40° C operating temperature range. Fused silica optics are commercially available that would satisfy the payload requirements. The BMC 6 x 6 (32 actuator) Mini deformable mirror options are summarized in Table 1, and only minor modifications to the driver board would be required. One possible option for a detector is an 8-bit 1/3" CMOS (Aptina) Imaging Development Systems (IDS) UI-1646 LE. The IDS UI-1646 LE weighs 12 g and is normally USB powered. The resolution is 1280 x 1024 with an optical size of 4.608 x 3.686 mm and pixel pitch of 3.6 μm.

4. SUMMARY AND FUTURE WORK

4.1 Summary

Direct imaging of an Earth-like exoplanet requires an imaging system capable of achieving contrasts of 1×10^{-10}. Such a contrast can be obtained through the use of active optics systems operated on space telescopes. High actuator count deformable mirrors are a key technology for this application, but their technology readiness level must be increased before they can be viably incorporated into such missions. In this paper, we have shown that it is feasible to design a 3U CubeSat platform that can accommodate a MEMS deformable mirror demonstration experiment using COTS and CubeSat parts and components. Hardware lab bench tests of both the Shack-Hartmann and Michelson Interferometer payload options are in progress. Each option offers a simple payload architecture that would enable characterization of the on-orbit performance of the deformable mirror. The Shack-Hartmann payload design may be easier to use for wavefront reconstruction and, additionally, provides the opportunity to detect stars as well as to use an internal light source for calibration and characterization.

4.2 Future work: Follow-on missions

There are several different follow-on opportunities that could be pursued as a result of this simple deformable mirror demonstration. One of the more interesting options would be to use the same platform for a different small deformable mirror and driver for comparison. Next steps would involve incorporating a compact external-viewing camera system that is imaging (and tracking) an astronomical object. The long-term goal is to enable the use of small deformable mirrors for space imaging and free space communication applications on any size payload and spacecraft.

5. ACKNOWLEDGMENTS

The authors would like to acknowledge support from the NASA Office of the Chief Technologist NASA Space Technology Research Fellowships (OCT-NSTRF), the Jeptha and Emily Wade Fund, and the MIT Undergraduate Research Opportunities Program (UROP). The authors also appreciate insightful discussions with Michael Feinberg, Dr. Steven Cornelissen, and Dr. Paul Bierden at Boston Micromachines, Inc., Dr. Wes Traub and Dr. John Trauger at NASA JPL, Prof. N. Jeremy Kasdin and Tyler Groff at Princeton University, Dr. Ruslan Belikov at NASA Ames Research Center, Prof. David Miller, Christopher Pong, and Matt Smith at MIT, Dr. Don Gavel and Andrew Norton at UCSC.

6. REFERENCES

[1] A. Wolszcan and D. Frail, "A planetary system around the millisecond pulsar PSR1257+12," *Nature*, vol. 355, no. 6356, pp. 145-147, 1992.

[2] Michel Mayor and Didier Queloz, "A Jupiter-mass companion to a solar-type star," *Nature*, vol. 378, pp. 355-359, 1995.

[3] N.J. Kasdin, R. Vanderbei, D. Spergel, and M. Littman, "Extrasolar planet finding via optimized apodized pupil and shaped pupil coronagraphs," *Astrophysical Journal*, vol. 582, p. 1147, 2003.

[4] X. Bonfils et al., "The HARPS search for southern extra-solar planets VI: A Neptune-mass planet around the nearby M dwarf Gl 581," *Astronomy and Astrophysics Letters*, vol. 443, no. 3, pp. L15-L18, 2005.

[5] W. Borucki, D. G. Koch, N. Batalha, and et al., "Kepler-22b: A 2.4 Earth radius planet in the habitable zone of a sun-like star," *Astrophysical Journal*, vol. 745, no. 2, p. 120, 2012.

[6] M. Tuomi et al., "Signals embedded in the radial velocity noise. Periodic variations in the tau Ceti velocities," *Astronomy and Astrophysics*, 2012, doi:10/1051/0004-6361/201220509.

[7] E. Palle, M. R. Zapatero Osorio, R. Barrena, P. Monanes-Rodriguez, and E. L. Martin, "Earth's transmission spectrum from lunar eclipse observations," *Nature*, vol. 459, no. 7248, pp. 814-816, 2009.

[8] M. S. Marley, J. Fortney, S. Seager, and T. Barman, *Protostars and Planets V*, B. Reipurth, D. Jewitt, and K. Keil, Eds. Tucson, AZ, USA: Univ. Arizona Press, 2007.

[9] J. J. Fortney, K. Lodders, M. S. Marley, and R. S. Freedman, "A unified theory for the atmospheres of the hot and very hot Jupiters: Two classes of irradiated atmospheres," *Astrophysical Journal*, vol. 678, pp. 1419-1435, 2008.

[10] E. Miller-Ricci, D. Sasselov, and S. Seager, "The atmospheric signatures of super Earths: How to distinguish between hydrogen-rich and hydrogen-poor atmospheres," *Astrophysical Journal*, vol. 690, p. 1056, 2009.

[11] L. Kaltenegger, W. Traub, and K. Jucks, "Spectral evolution of an Earth-like planet," *Astrophysical Journal*, vol. 658, no. 1, pp. 598-616, 2007.

[12] K. Cahoy, M. S. Marley, J. J. Fortney, R. Freedman, and K. Lodders, "Exoplanet albedo spectra and colors as a function of orbital phase, separation, and metallicity," *Astrophysical Journal*, vol. 724, no. 189, 2010.

[13] A.-L. Maire et al., "Atmospheric characterization of cold exoplanets using a 1.5-m coronagraphci space telescope," *Astronomy & Astrophysics*, vol. 541, no. A83, 2012.

[14] B. Benneke and S. Seager, "Atmospheric Retrieval for Super-Earths: Uniquely Constraining the Atmospheric Composition with Transmission Spectroscopy," *Astrophysical Journal*, vol. 753, no. 2, 2012.

[15] R. Hu, B. Ehlmann, and S. Seager, "Theoretical spectra of terrestrial exoplanet surfaces," *Astrophysical Journal*, vol. 752, no. 1, 2012.

[16] M. Kuchner and W. Traub, "A coronagraph with a band-limited mask for finding terrestrial planets," *Astrophysical Journal*, vol. 570, p. 200.

[17] O. Guyon et al., "Exoplanet imaging with a Phase-induced Amplitude Apodization Coronagraph. I. Principle," *Astrophysical Journal*, vol. 622, p. 744, 2005.

[18] E. Serabyn, D. Mawet, and R. Burruss, "An image of an exoplanet separated by two diffraction beamwidths from a star," *Nature*, vol. 464, no. 7291, pp. 1018-1020, 2010.

[19] D. Mawet et al., "The Vector Vortex Coronagraph: Laboratory Results and First Light at Palomar Observatory," *Astrophysical Journal*, vol. 709, no. 1, pp. 53-57, 2010.

[20] P. Deroo, M. Swain, and R. Green, "Spectroscopy of exoplanet atmospheres with the FINESSE Explorer mission," in *Space Telescopes and Instrumentation 2012: Optical, Infrared and Millimeter Wave*, vol. 8442, 2012, 844241-844141-9.

[21] W. Cash et al., "External occulters for direct observation of exoplanets: an overview," in *UV/Optical/IR Space Telescopes: Innovative Technologies and Concepts III*, vol. 6687, 2007, pp. 668712-668712-14.

[22] R. G. Lyon et al., "Visible nulling coronagraphy for Exo-Planetary detection and characterization," in *Direct Imaging of Exoplanets: Science & Techniques*, vol. 200, Cambridge, 2006, pp. 345-352.

[23] D. Defrere, C. Stark, K. Cahoy, and I. Beerer, "Direct imaging of exoEarths embedded in clumpy debris disks," in *Space Telescopes and Instrumentation 2012: Optical, Infrared, and Millimeter Wave*, vol. 8442, 2012, pp. 84420M-84420M-8.

[24] V. V. Sobolev, *Light Scattering in Planetary Atmospheres*, International Series of Monographs in Natural Philosophy ed.: Elsevier, 1975, vol. 76.

[25] Correia, C., H.F. Raynaud, C. Kulcsar, and J.-M. Conan, "On the optimal reconstruction and control of adaptive optics systems with mirror dynamics," *JOSA A*, vol. 27, no. 2, pp. 333-349, 2010.

[26] R. Angel, "Ground based imaging of extrasolar planets using adaptive optics," *Nature*, vol. 368, pp. 203-207, 1994.

[27] A. Sivaramakrishnan, J. Lloyd,. Hodge, and B. Macintosh, "Speckle decorrelation and dynamic range in speckle

noise limited ranging," *Astrophysical Journal*, vol. 581, no. L59, 2002.

[28] M. Perrin, A. Sivaramakrishnan, R. Makidon, B. Oppenheimer, and J. Graham, "The structure of high strehl ratio point-spread functions," *Astrophysical Journal*, vol. 596, p. 702, 2003.

[29] B. Macintosh et al., "The Gemini Planet Imager: From science design to construction," in *Proc. SPIE*, pp. 7015-18.

[30] O. Guyon, T. Matsuo, and R. Angel, "Coronagraphic low-order wavefront sensor: Principle and application to a Phase-Induced Amplitude Apodization coronagraph," *Astrophysical Journal*, vol. 693, p. 75, 2009.

[31] J. Puig-Suari, C. Turner, and R. Twiggs, "CubeSat: the development and launch support infrastructure for eighteen different satellite customers on one launch," in *Small Satellite*, pp. SSC01-VIIIb-5.

[32] Robert K. Tyson, *Principles of Adaptive Optics*. Boca Raton, FL, USA: CRC Press, 2011.

[33] F. Martinache, "The asymmetric pupil Fourier wavefront sensor," *submitted to the Proceedings of the Astronomical Society of the Pacific*, 2013.

[34] Matthew W. Smith et al., "ExoplanetSat: Detecting transiting exoplanets using a low-cost CubeSat platform," in *Proc. SPIE*, vol. 7731, pp. 773127-1.

[35] Christopher Pong et al., "Achieving high-precision pointing on ExoplanetSat: initial feasibility analysis," in *Proc. SPIE*, vol. 7731, 2010, p. 7731V, doi:10.1117/12.857992.

[36] C. Mendillo, S. Chakrabarti, T. Cook, and B. Hicks, "Flight demonstration of a milliarcsecond optical pointing system for direct exoplanet imaging," in *American Astronomical Society*, 2009, p. 446.03.

[37] X. Wu, L. Yao, and H. Ou, "Novel hierarchically dimensioned deformable mirrors with integrated ASIC driver electronics," in *SPIE MOEMS-MEMS*, 2012.

[38] J. Stewart. (2009) Compact low power driver for deformable mirror systems.

[39] Boston Micromachines Corporation, "Deformable Mirrors," 2011.

[40] Thorlabs Inc. Thorlabs Adaptive Optics Kits. [Online]. http://thorlabs.com/thorcat/18100/DM32-35-UM01-AutoCADPDF.pdf

[41] R. N. Smartt and J. Strong, "Point-diffraction Interferometer," *Journal of the Optical Society of America*, vol. 62, p. 737, 1974.

[42] Frank Traeger, *Springer handbook of lasers and optics*. New York: Springer, 2007.

[43] W. Demtroeder, *Laser spectroscopy, basic concepts and instrumentation*, 3rd ed. Berlin: Springer-Verlag, 2003.

[44] C. Scheiner, "Oculus, sive fundamentum opticum," 1619.

[45] J. Springmann, A. Sloboda, A. Klesh, M. Bennett, and J. Cutler, "The attitude determination system of the RAX satellite," *Acta Astronautica*, vol. 75, pp. 120-135, 2012.

[46] C. Ting, D.G. Voelz, and M.K. Giles, "Laser satellite communications with adaptive optics," in *Proc. SPIE*, vol. 5892, 2005.

[47] D.E. Smith et al., "Two way laser link over interplanetary distance," *Science*, vol. 311, no. 53, p. 5757, 2006.

[48] H. Shea, "Reliability of MEMS for space applications," in *Proc. SPIE*, 2006.

[49] O. Guyon et al., "Detecting and characterizing exoplanets with a 1.4-m space telescope: The Pupil-mapping Exoplanet Coronagraphic Explorer (PECO)," in *Proc. SPIE*, 2009, p. 74400.

[50] R. Duffner, *The Adaptive Optics Revolution: A History*. Albuquerque, NM: University of New Mexico Press, 2009.

[51] K. Cahoy et al., "Science performance of the Pupil-mapping Exoplanet Coronagraphic Observer (PECO)," in *Proc. SPIE*, 2009, p. 74400.

[52] J. Achenbach. (2012, June) NASA gets two military spy telescopes for astronomy.

[53] Christopher Mendillo, Supriya Chakrabarti, Timothy Cook, Brian Hicks, and Benjamin Lane, "Flight demonstration of a milliarcsecond pointing system for direct exoplanet imaging," *Applied Optics*, vol. 51, no. 29, pp. 7069-7079, 2012.